Monthly Notices of the ROYAL ASTRONOMICAL SOCIETY

MNRAS **510,** 858–869 (2022) https://doi.org/10.1093/mnras/stab3487
Advance Access publication 2021 December 2

Uncovering the chemical structure of the pulsating low-mass white dwarf SDSS J115219.99+024814.4

A. D. Romero [1]★ G. R. Lauffer [1] A. G. Istrate [2] and S. G. Parsons [3]

[1]*Physics Institute, Universidade Federal do Rio Grande do Sul, Avenida Bento Goncalves 9500, Porto Alegre 91501-970, RS, Brazil*
[2]*Department of Astrophysics, Radboud University Nijmegen, P.O. Box 9010, Nijmegen NL-6500 GL, the Netherlands*
[3]*Department of Physics and Astronomy, University of Sheffield, Sheffield, S3 7RH, UK*

Accepted 2021 November 26. Received 2021 October 22; in original form 2021 March 14

ABSTRACT

Pulsating low-mass white dwarf (WD) stars are WDs with stellar masses between 0.30 and 0.45 $M_\odot$ that show photometric variability due to gravity-mode pulsations. Within this mass range, they can harbour both a helium core and hybrid core, depending if the progenitor experienced helium-core burning during the pre-WD evolution. SDSS J115219.99+024814.4 is an eclipsing binary system where both components are low-mass WDs, with stellar masses of 0.362 ± 0.014 $M_\odot$ and 0.325 ± 0.013 $M_\odot$. In particular, the less-massive component is a pulsating star, showing at least three pulsation periods of ∼1314, ∼1069, and ∼582.9 s. This opens the way to use asteroseismology as a tool to uncover its inner chemical structure, in combination with the information obtained using the light-curve modelling of the eclipses. To this end, using binary evolutionary models leading to helium- and hybrid-core WDs, we compute adiabatic pulsations for $\ell = 1$ and $\ell = 2$ gravity modes with `Gyre`. We found that the pulsating component of the SDSS J115219.99+024814.4 system must have a hydrogen envelope thinner than the value obtained from binary evolution computations, independently of the inner composition. Finally, from our asteroseismological study, we find a best-fitting model characterized by $T_{\rm eff} = 10\,917$ K, $M = 0.338$ $M_\odot$, and $M_{\rm H} = 10^{-6}$ $M_\odot$ with the inner composition of a hybrid WD.

Key words: asteroseismology – binaries: eclipsing – white dwarfs.

1 INTRODUCTION

White dwarfs (WDs) are the most common endpoint of stellar evolution. All stars with initial masses below 7−12 $M_\odot$ (e.g. Garcia-Berro, Isern & Hernanz 1997; Woosley & Heger 2015; Lauffer, Romero & Kepler 2018), representing more than 95 per cent of the stars in the Milky Way, will end their lives as WDs. The WD population can be divided into hydrogen (H)-rich atmosphere objects (DA), that correspond to more than 85 per cent of all WDs, and H-deficient objects (non-DA), which show no H in their atmospheres (see Fontaine & Brassard 2008; Althaus et al. 2010a).

For H-atmosphere WDs the mass distribution peaks at ∼0.6 $M_\odot$, which represents ∼84 per cent of the total sample (Kepler et al. 2007; Kepler et al. 2015), exhibiting also a high- and a low-mass components. The low- and high-mass WDs are most likely the result of close binary evolution, where mass transfer and mergers commonly occur.

The low-mass tail in the DA mass distribution peaks at ∼0.39 $M_\odot$ and extends to stellar masses <0.45 $M_\odot$. WDs with masses <∼0.30 $M_\odot$ can only be formed through mass transfer in close binary systems, since single star evolution is not able to form such remnants in the Hubble time (Kilic, Stanek & Pinsonneault 2007; Istrate et al. 2016; Pelisoli & Vos 2019). These objects are known as extremely low-mass white dwarfs (ELMs). Low-mass WDs are stars with stellar masses in the range of $0.30 \leq M/M_\odot \leq 0.45$. In addition to the binary formation channel, these objects could also form as a result of strong mass-loss episodes during giant stages for high-metallicity progenitors. Noteworthy, low-mass WDs can harbour either a pure helium (He) core (e.g. Panei et al. 2007; Althaus, Miller Bertolami & Córsico 2013; Istrate, Tauris & Langer 2014; Istrate et al. 2016) or a hybrid core, composed of He, carbon (C), and oxygen (O; e.g. Iben & Tutukov 1985; Han, Tout & Eggleton 2000; Prada Moroni & Straniero 2009; Zenati, Toonen & Perets 2019).

Probably the only way to probe the inner chemical composition in detail is through the pulsation-period spectrum observed in variable stars. Each pulsation mode propagates in a specific region providing information on that particular zone, where its amplitude is maximum (Tassoul, Fontaine & Winget 1990). Thus, we can perform an asteroseismic study, where we compare the observed periods with the theoretical period spectrum, computed using representative models, to uncover the inner stellar structure (see e. g. Romero et al. 2012, 2019).

There are currently several families of pulsating WDs that can be found in specific ranges of effective temperature and surface gravity. They show g-mode non-radial pulsations with periods range from minutes to a few hours and variation amplitudes of millimag. The excitation mechanism acting on pulsating WDs is a combination of the κ-mechanism, driven by an opacity bump due to partial ionization of the main element in the outer layers (Dolez & Vauclair 1981; Winget et al. 1982), and the γ-mechanism, related to the effect of a small value of the adiabatic exponent in the ionization zone (Brickhill 1991; Goldreich & Wu 1999).

The location of the different classes in the Kiel diagram is depicted in Fig. 1. At high effective temperatures we find the GW

★ E-mail: alejandra.romero@ufrgs.br

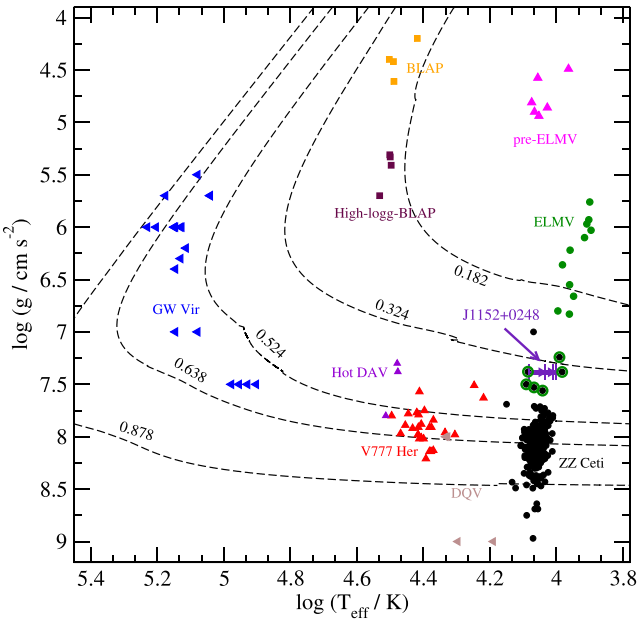

Figure 1. The classes of pulsating WDs. The data were extracted from Fontaine & Brassard (2008), Bognar & Sodor (2016), Pietrukowicz et al. (2017), Córsico et al. (2019), Romero et al. (2019), and Kupfer et al. (2019). For reference, we include theoretical WD sequences with C/O core and masses of 0.878, 0.638, and 0.524 $M_\odot$ (Romero, Campos & Kepler 2015) and He-core with stellar mass of 0.324 and 0.182 $M_\odot$ (Istrate et al. 2016). The different symbols indicate the element related to the excitation mechanism: H (circles), He (triangle-up), C and/or O (triangle-left), and iron peak elements (squares). The known variable low-mass WDs are indicated with a surrounding green circle. The position of J115219.99+024814.4 is depicted with a triangle-right, with the atmospheric parameters taken from Parsons et al. (2020; see Table 1 for details).

Vir stars, with C/O atmospheres, followed by He-rich atmosphere V777 Her and the C-rich atmosphere DQV. Finally, the H-envelope pulsating WDs, known as ZZ Ceti stars, are located at lower effective temperatures. For lower log (g), we find the pulsating low-mass WDs, and the ELMs along with their progenitors, the pre-ELMs. Even though the group of pulsating ELMs is considered a class on its own, their instability strip is an extension of the ZZ Ceti instability strip to lower surface gravities, as can be seen from Fig. 1.

There are 11 pulsating ELMs known to date (green dots in Fig. 1, Hermes et al. 2013a, b; Bell et al. 2015, 2017; Kilic et al. 2015; Pelisoli et al. 2018). The pulsating ELMs are characterized by periods in the range of 100−6 300 s, effective temperatures of 7 800−10 000 K, and an H-dominated surface composition (Córsico et al. 2019). In addition, there are 10 objects in the literature with stellar masses within the range $0.30 \leq M/M_\odot \leq 0.45$ (black-green dots in Fig. 1) that show photometric variability with periods between 200 and 1300 s (Bognar & Sodor 2016; Fuchs 2017; Su et al. 2017; Rowan et al. 2019). For four of them, the uncertainties in the atmospheric parameters are quite large, leading to an uncertainty in stellar mass of 0.1–0.4 $M_\odot$ (Su et al. 2017; Rowan et al. 2019). The low number of pulsating low-mass WDs as compared to canonical mass ZZ Ceti stars could be due to some kind of fine tuning during the evolution of the progenitor, but it is most likely due to the lack of studies focused on the search for pulsations for objects in this stellar mass range.

Recently, Parsons et al. (2020) reported the discovery of the first pulsating low-mass WDs in a compact eclipsing binary system (orbital period of 2.4 h), which happens to have another low-mass WD as a companion. The binary nature of the SDSS J115219.99+024814.4 system (hereafter J1152+0248) was first reported by Hallakoun et al. (2016), based on K2 data from the *Kepler* mission. Parsons et al. (2020) performed high-speed photometry observations with HiPERCAM on the 10.4 m *Gran Telescopio Canárias* in five different bands, with a total of 108 min of data, covering both primary and secondary eclipses. From the high time-resolution light curves they found pulsation-related variations from the cooler component with at least three significant periods. To determine the mass and radius of each component in J1152+0248, they combine radial velocity determinations from X-shooter spectroscopy with the information extracted from the primary and secondary eclipses in the light curves (see their table 1). The effective temperature was determined using two techniques, i.e. by fitting the spectral energy distribution [$T_{\rm eff}$ (SED)] and by modelling the light curves including the effects of the eclipses [$T_{\rm eff}$ (eclipse)]. The stellar parameters obtained by Parsons et al. (2020) for the pulsating component in J1152+0248 (hereafter J1152+0248 −V) are listed in Table 1.

Table 1. Stellar parameters presented in Parsons et al. (2020) for the pulsating component of the J1152+0248 eclipsing binary.

Parameter	Value
$M_*/M_\odot$	0.325 ± 0.013
$R_*/R_\odot$	0.0191 ± 0.0004
log $[g/(\mathrm{g\ cm^{-2}})]$	7.386 ± 0.012
$T_{\rm eff}$/K (SED)	$11\,100^{+950}_{-770}$
$T_{\rm eff}$/K (eclipse)	$10\,400^{+400}_{-340}$

Based on the determination of the radius, Parsons et al. (2020) proposed that J1152+0248 −V is either a hybrid- or an He-core low-mass WD with an extremely thin surface H layer ($M_{\rm H}/M_\odot < 10^{-8}$). Different inner chemical structures will influence the characteristic period spectrum of a pulsating star. Therefore, an asteroseismological study of this object can shed some light on both the chemical composition and the mass of the H envelope.

In this work, we explore the pulsational properties of both hybrid- and He-core low-mass WD models representative for the case of J1152+0248 −V. Furthermore, we consider sequences with H envelopes thinner than the value predicted by stable mass-transfer binary evolutionary models. For the evolutionary computations we use the stellar evolution code MESA (Paxton et al. 2011, 2013, 2015, 2018, 2019), while the adiabatic pulsations are computed using GYRE stellar oscillation code (Townsend & Teitler 2013; Townsend, Goldstein & Zweibel 2018). Using the theoretical period spectra, we perform an asteroseismological study of J1152+0248 −V to uncover its inner structure.

This paper is organized as follows. In Section 2, we provide a description of the evolutionary computations and the input physics adopted in our calculations. In Section 3, we present the pulsation computations. Section 4 is devoted to study the pulsational properties of our low-mass WD models, including a comparison between the hybrid- and He-core configurations. The results of the asteroseismological study of J1152+0248 −V are presented in this section as well. Our final remarks are presented in Section 5.

2 EVOLUTIONARY SEQUENCES

The evolutionary models presented in this work are computed using the open-source binary stellar evolution code MESA (Paxton et al. 2011, 2013, 2015, 2018, 2019) version 12115 and are part of a grid of

models covering the mass interval where He- and hybrid-core WDs overlap, i.e. ∼0.32–0.45 $M_\odot$ (Istrate et al., in preparation). Since the aim of this work is analyse the core composition of J1152+0248 −V using asteroseismology, we only consider sequences compatible with its observed effective temperature and radius. We present evolutionary sequences for a WD mass of 0.325 $M_\odot$, corresponding to the value obtained by Parsons et al. (2020), and 0.338 $M_\odot$, i.e. the maximum WD mass compatible within 1σ.

2.1 Input physics

We compute binary evolutionary sequences using similar assumptions as in Istrate et al. (2016). All models include rotation, with the initial rotational velocity initialized such that the donor is synchronized with the orbital period. We include magnetic braking for the loss of angular momentum just for the donors leading to the formation of the He-core WDs. For more massive donors (>2.0 $M_\odot$), which are considered for the progenitors of the hybrid-core WDs, we assume that the magnetic braking stops operating. This assumption follows from the conventional thinking that braking via a magnetized stellar wind is inoperative in stars with radiative envelopes (Kawaler 1988). For all the models, we assume a mass-transfer efficiency of 50 per cent, i.e. 50 per cent of the transferred mass is accreted by the companion, while the rest leaves the system with the specific angular momentum of the accretor.

Below, we briefly describe the main input physics considered in the evolutionary computations and refer to Istrate et al. (in preparation) for more details. We consider an initial metallicity of $Z = 0.01$, with an He abundance given by $Y = 0.24+2.0 \cdot Z$ and the metal abundances scaled according to Grevesse & Sauval (1998). Convection is modelled using the standard mixing-length theory (Henyey, Vardya & Bodenheimer 1965) with a mixing-length parameter $\alpha = 2.0$, adopting the Ledoux criterion. A step function overshooting extends the mixing region for 0.25 pressure scale heights beyond the convective boundary during core H burning. In order to smooth the boundaries we also include exponential overshooting with $f = 0.0005$. Semiconvection follows the work of Langer, Fricke & Sugimoto (1983), with an efficiency parameter $\alpha_{sc} = 0.001$. Thermohaline mixing is included with an efficiency parameter of 1.0. Radiative opacities are taken from Ferguson et al. (2005) for $2.7 \leq \log T \leq 3.8$ and OPAL (Iglesias & Rogers 1993, 1996) for $3.75 \leq \log T \leq 8.7$, and conductive opacities are adopted from Cassisi et al. (2007).

The nuclear network used is *cno_extras.net* which accounts for additional nuclear reactions for the CNO burning compared to the default *basic.net* network. We consider the effects of element diffusion (e.g. Iben & Tutukov 1985; Thoul, Bahcall & Loeb 1994) on all isotopes and during all the stages of evolution.

We adopt a grey atmosphere using the Eddington approximation on the evolution prior to the cooling track, and the WD atmosphere tables from Rohrmann et al. (2012) during the WD cooling stage.

Rotational mixing and angular momentum transport are treated as diffusive processes as described in Heger, Langer & Woosley (2000), with an efficiency parameter $f_c = 1/30$ (Chaboyer & Zahn 1992) and a sensitivity to composition gradients parametrized by $f_\mu = 0.05$. We also include transport of angular momentum due to electron viscosity (Itoh, Kohyama & Takeuchi 1987).

2.2 WD formation history

Fig. 2 shows the evolution of the donor star in the Kiel diagram leading to a remnant mass of 0.338 $M_\odot$ with an He core (solid orange line) and hybrid core (blue dashed line). The evolution is computed from the zero-age main sequence (ZAMS) until the remnant WD cools down to an effective temperature of 5 000 K. In both cases, the companion star is treated as a point mass. We also mark on the evolutionary sequences several important points. The moment when the donor star overflow its Roche lobe (RLOF), marking the beginning of the mass-transfer phase, is depicted with a circle symbol, the end of the mass-transfer phase is marked with a star, the beginning and the end of the core-He burning phase are showed with the square and thin diamond symbol, respectively. Finally, the beginning of the cooling track is represented by the diamond symbol.

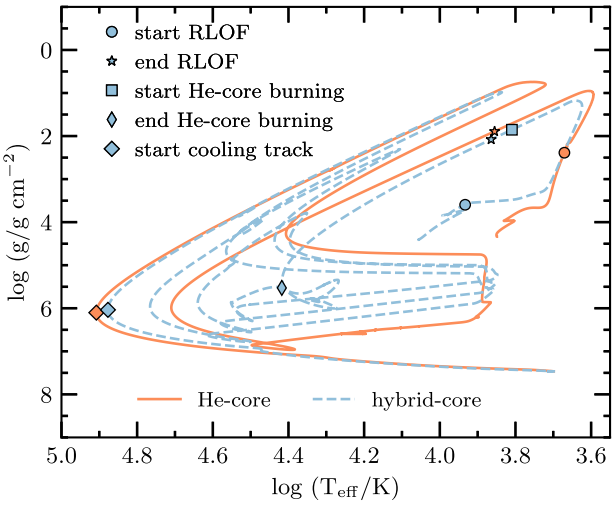

Figure 2. The Kiel diagram showing the formation and the cooling evolution of a 0.338 $M_\odot$ He- (solid orange line) and hybrid-core (dashed blue line) WD. The initial binary parameters are $M_{donor} = 1.3$ $M_\odot$, $M_{accretor} = 1.2$ $M_\odot$, $P_{initial} = \sim 16.982$ d for the He-core model, and $M_{donor} = 2.3$ $M_\odot$, $M_{accretor} = 2.0$ $M_\odot$, $P_{initial} = \sim 1.990$ d for the hybrid-core model, at an initial metallicity of $Z = 0.01$. In both cases, the accretor is treated as a point mass. The evolutionary tracks are computed from ZAMS until the effective temperature of the WD reaches 5 000 K. The symbols mark various stages of evolution. The beginning and the end of the mass-transfer phase are represented by the circle and star symbol, respectively, the beginning and the end of the core-He burning phase (in the case of the hybrid-core sequence) are depicted by the square and thin diamond symbol, respectively, and finally the diamond symbol represents the beginning of the cooling track, i.e. the point when the evolutionary track reaches its maximum effective temperature.

The He-core WDs are formed by stripping mass when the donor star is on its red giant branch. The binary system consists of a low-mass donor star with an initial mass of 1.3 $M_\odot$, a main-sequence companion of 1.2 $M_\odot$, and an initial orbital period of ∼11.75 and ∼16.98 d, for the progenitor of the 0.325 $M_\odot$ and 0.338 $M_\odot$, respectively. After the end of the mass-transfer phase, the remnant evolves through the so-called proto-WD phase, in which unstable H burning leads to the occurrence of at least one H flash.

The initial binary configuration leading to the formation of the hybrid-core WDs is a 2.3 $M_\odot$ intermediate-mass donor star with a companion of 2.0 $M_\odot$, and an orbital period of 1.43 and ∼1.99 d, or the progenitor of the 0.325 $M_\odot$ and 0.338 $M_\odot$, respectively. The mass-transfer phase initiates during the Hertzsprung gap. Unlike the case of the He-core WD sequence, here the mass transfer ceases due to the core-He ignition. Shortly after the mass transfer ended, the remnant starts the core-He burning phase, which lasts around 670 Myr. Once the CO core is formed, the proto-WD undergoes four H shell flashes before finally settling on the cooling track.

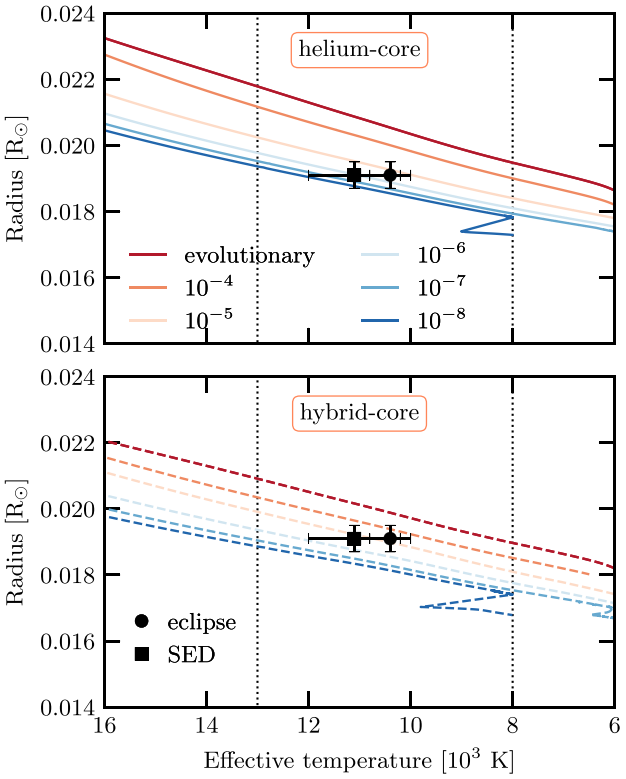

Figure 3. Stellar radius as a function of the effective temperature for both hybrid- (dashed lines) and He-core (solid lines) WD sequences with stellar mass 0.338 M$_\odot$. The symbols correspond to the determinations of the effective temperature from observations (see Table 1). The dotted vertical lines indicate the blue and red edges of the observed instability strip for low-mass WDs (see Fig. 1).

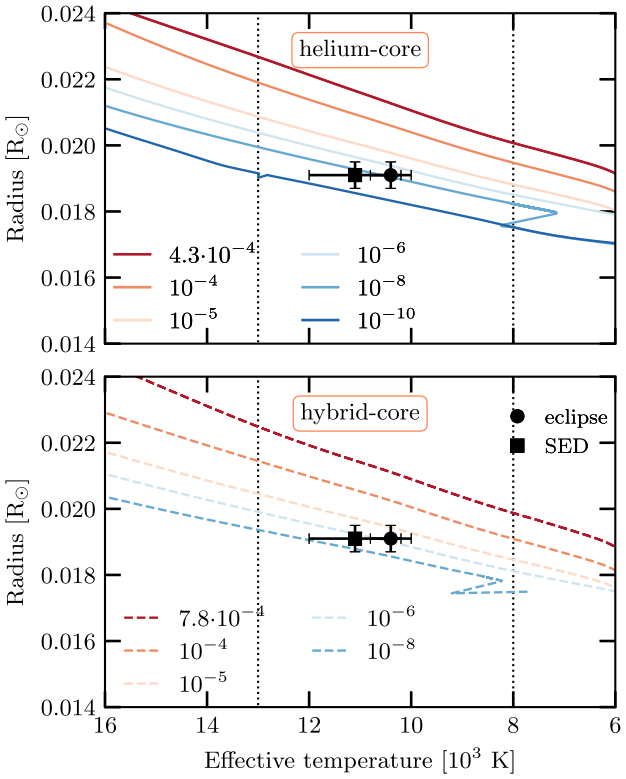

Figure 4. Same as Fig. 3 but for the WD sequences with stellar mass 0.325 M$_\odot$.

2.3 WD cooling track

The WD sequences discussed in the previous section are formed through a stable mass-transfer channel. While it is possible that the first mass-transfer phase which leads to the formation of J1152+0248 −V is stable, we cannot rule out completely a common-envelope evolution. Additionally, the short orbital period of J1152+0248 (2.4 h) suggests that the second mass-transfer phase leading to the formation of the most massive component is unstable and proceeds through a common-envelope evolution. This evolutionary phase could possibly also affect the lower-mass component. Either way, there is an uncertainty in the mass of the H envelope available at the beginning of the cooling track resulting from the evolutionary history prior to the observed stage of the system.

The mass of the H envelope is one of the main factors that influence the cooling evolution of a WD. In order to take this uncertainty into account, we also computed WD cooling sequences with H envelopes thinner than the ones obtained from the binary evolutionary models described above. These sequences were computed using *relaxation* methods available in MESA. The initial conditions are taken at the point when the remnant reaches the beginning of the cooling track. Using the stellar profile at this point, we remove the desired amount of H, keeping the total mass unchanged (see Istrate et al., in preparation, for details).

Figs 3 and 4 show the WD radius as a function of the effective temperature for sequences with He- (top panels) and hybrid-core (bottom panels) and stellar mass of 0.338 M$_\odot$ and 0.325 M$_\odot$, respectively.

For each core composition we consider different values of the H-envelope mass, starting from the value resulting from the binary evolution down to 10^{-8} M$_\odot$. In particular, for the stellar mass of 0.325 M$_\odot$ and He core, we also include a sequence with H-envelope mass of 10^{-10} M$_\odot$. Overplotted are the measured values of J1152+0248 −V, both from the eclipse and the SED fitting.

As expected, the radius for the hybrid-core sequences is smaller than for the He-core sequences, for the same H-envelope mass. Intriguingly, the observations are not compatible with a thick H envelope, i.e. which obtained from binary evolution computations. For sequences characterized with a stellar mass of 0.338 M$_\odot$ (see Fig. 3) the H-envelope mass consistent with the radius and effective temperature from Parsons et al. (2020) is between 10^{-4} and 10^{-6} M$_\odot$ if we consider a hybrid core. For the sequences with an He core, the H-envelope mass is below 10^{-5} M$_\odot$. For sequences with stellar mass of 0.325 M$_\odot$ (see Fig. 4), the H-envelope mass needs to be even smaller to fit the observations, between 10^{-5} and 10^{-8} M$_\odot$ for sequences with a hybrid core and between 10^{-5} and 10^{-10} M$_\odot$ for sequences with an He core. Thus, J1152+0248 −V has an H envelope thinner than that obtained from evolutionary sequences, independently of the central chemical composition.

3 ADIABATIC PULSATIONS

The pulsational properties in stars are dominated by the characteristic frequencies, i.e. the Brunt-Väisälä (N^2) and the Lamb (L_ℓ^2) frequencies (Cowling 1941; Unno et al. 1989). The Brunt-Väisälä frequency represents the oscillation frequency of a convective bubble around the stable equilibrium position. It is closely related with gravity modes

since the restoring force is gravity. In the case of low-mass WDs, the gravity modes correspond to the long-period (low-frequency) modes, with periods $\gtrsim$200 s for $\ell = 1$. The N^2 frequency is given by (Brassard et al. 1991)

$$N^2 = \frac{g^2\rho}{P}\frac{\chi_T}{\chi_\rho}(\nabla_{\rm ad} - \nabla + B), \quad (1)$$

where g, ρ, and P are the gravitational acceleration, the density, and the pressure, respectively. $\nabla_{\rm ad}$ and ∇ are the adiabatic and the temperature gradient, respectively, and χ_T and χ_ρ are defined as,

$$\chi_T = \left(\frac{\partial \ln P}{\partial \ln T}\right)_\rho \quad (2)$$

$$\chi_\rho = \left(\frac{\partial \ln P}{\partial \ln \rho}\right)_T. \quad (3)$$

The term B is called the Ledoux term and it is defined as

$$B = -\frac{1}{\chi_T}\left(\frac{\partial \ln P}{\partial ln X_i}\right)_{\rho,T}\frac{{\rm d}\ln X_i}{{\rm d}\ln P}, \quad (4)$$

where X_i is the chemical abundance of the element i. The Ledoux term B gives the explicit contribution of the change of chemical composition, thus it contributes in the region where chemical transitions are found (Brassard et al. 1992a).

The Lamb frequency is given by

$$L_\ell^2 = \frac{(\ell+1)\ell}{r^2}c_{\rm S}^2, \quad (5)$$

where $c_{\rm S}$ is the adiabatic sound speed. The Lamb frequency is inversely proportional to the time that a sound wave takes to travel a distance $2\pi r/\ell$. It is closely related to pressure modes since the restoring force is the pressure gradient. Pressure modes correspond to short-period (high-frequency) modes with periods of $\lesssim$10 s for low-mass WDs.

For a chemically homogeneous and radiative star, the period spectrum is characterized by a constant period separation, known as the asymptotic period spacing (Tassoul, Fontaine & Winget 1990),

$$\Delta\Pi_a = \frac{\Pi_0}{[\ell(\ell+1)]^{1/2}}, \quad (6)$$

where

$$\Pi_0 = 2\pi^2\left(\int_{r_1}^{r_2}\frac{N(r)}{r}{\rm d}r\right)^{-1}. \quad (7)$$

In the case of WDs, the inner chemical structure is far from homogeneous, showing composition gradients (Althaus et al. 2010b). In this case, the asymptotic period spacing corresponds to the period spacing at the limit of very large values of k (Tassoul et al. 1990).

3.1 Numerical computations

For our pulsational computations we employed GYRE (Townsend & Teitler 2013; Townsend, Goldstein & Zweibel 2018), an open-source stellar oscillation code in its adiabatic form, version 5.0. Although GYRE is integrated within MESA, it was used as a stand-alone package. We performed a scan using a linear grid over a period range of 80−2000 s with alpha_osc = 100 and alpha_exp and alpha_ctr set to 50. The boundary conditions and variables were set to UNNO and DZIEM, respectively.[1]

[1]The inlist and all its configuration settings can be found in here (link to be updated).

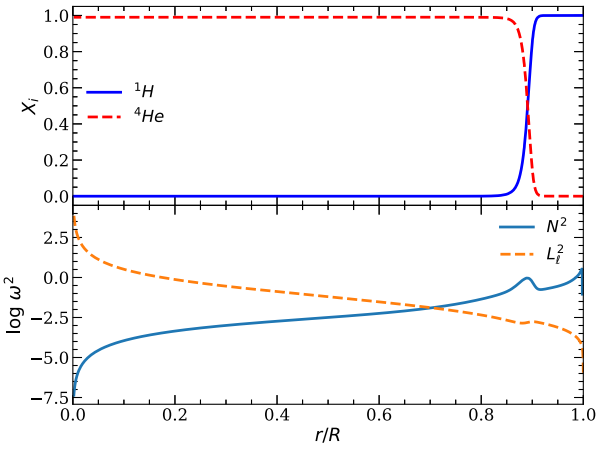

Figure 5. Internal profiles and characteristic frequencies for an *He-core* cooling sequence with M=0.338 $M_\odot$, $T_{\rm eff}$ = 10 000 K, and $M_{\rm H} = 10^{-4}$ $M_\odot$. Top panel: The mass fraction of H and He as a function of the relative radius. Bottom panel: The logarithm of the Brunt-Väisälä (full blue line) and the Lamb (dashed orange line) characteristic frequencies as a function of the relative radius.

We compute pulsations for He- and hybrid-core models in the effective temperature range of 13 000 and 8 000 K, which covers the empirical instability strip. We compute the period spectrum for $\ell = 1$ and $\ell = 2$ gravity modes with periods in a range of 80 s $\leq \Pi \leq$ 2 000 s.

3.2 Internal composition and the characteristic frequencies

To compare the pulsation properties of He- and hybrid-core WD models, we chose one template model for each central composition, with stellar mass of 0.338 $M_\odot$, effective temperature of 10 000 K, and H-envelope mass of 10^{-4} $M_\odot$. In the top panel of Figs 5 and 6, we depict the chemical profiles for an He- and a hybrid-core template models, respectively. Both template models show a pure H envelope, since gravitational settling had enough time to separate the elements in the outer layers. For the hybrid-core model we have a second chemical transition (He/C/O transition) around $r/R \sim 0.4$, where the He abundance decreases towards the centre while the C and O abundance increase.

The presence of chemical transitions, where the abundances of nuclear species vary considerably in radius, modifies the conditions of the resonant cavity in which modes should propagate as standing waves. Specifically, the chemical transitions act as reflecting walls, trapping certain modes in a particular region of the star, where they show larger oscillation amplitudes. Trapped modes are those for which the wavelength of their radial eigenfunction matches the spatial separation between two chemical transitions or between a transition and the stellar centre or surface (Brassard et al. 1992b; Bradley, Winget & Wood 1993; Córsico et al. 2002).

The bottom panels of Figs 5 and 6 show the run of the logarithm of the Brunt-Väisälä and Lamb frequencies as a function of radius for the template models. The overall behaviour of $\log N^2$ is a general decrease with increasing stellar depth, eventually reaching small values in the deep core, as a consequence of degeneracy. As expected, the bumps in $\log N^2$ correspond to the chemical transition, where the chemical gradients have non-negligible values (Tassoul et al. 1990). For the He-core template model, the Brunt-Väisälä frequency shows only one bump corresponding to the H/He transition at $r/R \sim 0.9$. For the hybrid-core template model, in addition to the bump

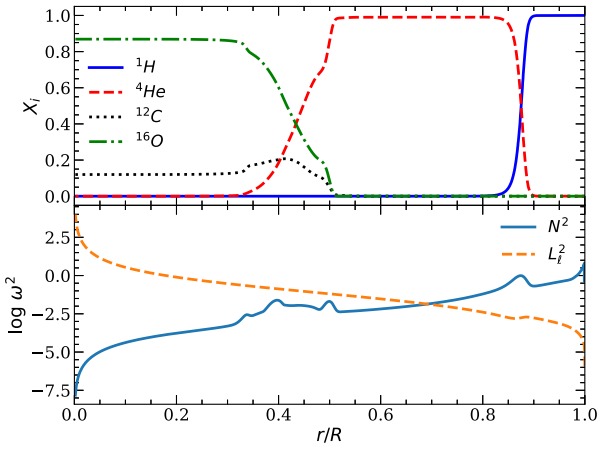

Figure 6. Internal chemical composition and characteristic frequencies for a *hybrid-core* sequence with M=0.338 $M_\odot$, $T_{\rm eff}$ = 10 000 K, and $M_{\rm H} = 10^{-4}$ $M_\odot$. Top panel: Mass fraction of H, He, C, and O as a function of the relative radius. *Bottom* panel: The logarithm of the Brunt-Väisälä (full blue line) and Lamb (dashed orange line) characteristic frequencies as a function of the relative radius.

at the base of the H envelope, the Brunt-Väisälä frequency shows a structure corresponding to the He/C/O transition around $r/R \sim 0.4$. This transition is wide and shows three peaks due to the structure of the chemical gradients. We expect that the different profiles for the Brunt-Väisälä frequency for He-core and hybrid-core models will impact the pulsation properties, for example the period spectrum and the period spacing.

The Lamb frequency is only sensitive to the H/He transition at the bottom of the H envelope, as it is the case for ZZ Ceti stars (Romero et al. 2012). Thus, we do not believe the pressure modes could give information on the inner regions, if ever detected in low-mass WD stars.

4 RESULTS

4.1 Pulsational properties

As previously mentioned, for a chemically homogeneous and radiative star, the forward period spacing ($\Delta\Pi_k = \Pi_{k+1} - \Pi_k$) would be constant and given by the asymptotic period spacing, defined in equation (6). However, in the stratified inner structures, as the ones found in low-mass WDs, the forward period spacing deviates from a constant value, particularly for low-radial order modes. In this section, we will focus on models with stellar mass 0.338 $M_\odot$. Similar results are found for models with stellar mass of 0.325 $M_\odot$.

Fig. 7 shows the forward period spacing as a function of the period for $\ell = 1$ modes. Top panels correspond to models with He core while bottom panels show the results for hybrid-core models. Finally, each column corresponds to sequences with different values for the H-envelope mass and each curve shows the forward period spacing at a different effective temperature along the cooling curve, from 12 000 K to 9000 K.

For the He-core models the distribution for the forward period spacing as a function of the period, shows a simple trapping cycle characteristic of one-transition models (Brassard et al. 1992b; Córsico & Althaus 2014), with defined local minima, as shown in the top panels of Fig. 7. For the hybrid-core models (bottom panels in Fig. 7) the pattern in the forward period spacing is more complex largely due to the influence of the He/C/O transition in the Brunt-Vaisälä frequency. Even though we expect the H/He transition to be dominant in the mode selection process, the presence of the second, broader, transition is not negligible. The differences in the pattern of the forward period spacing can be used to determine the inner composition of low-mass WDs, if enough consecutive periods are detected.

The trapping period, i.e. the period difference between two consecutive minima in $\Delta\Pi_k$, is longer for lower effective temperatures and thinner H envelopes. This effect is much more evident for the He-core models than for the hybrid-core models.

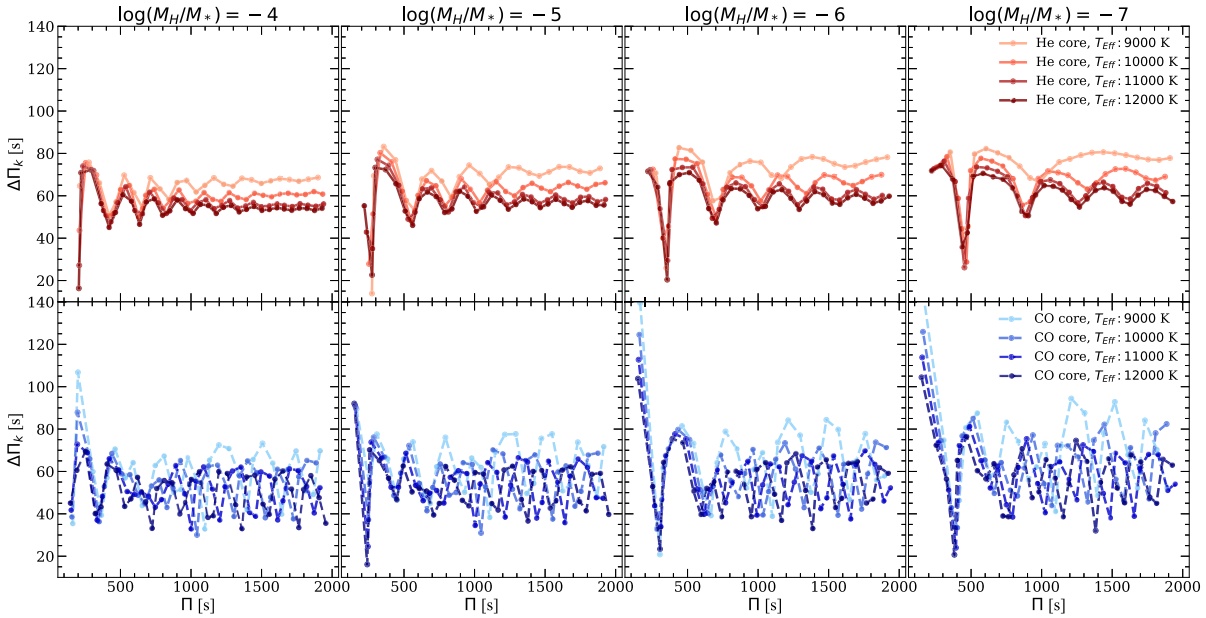

Figure 7. The forward period spacing ($\Delta\Pi_k = \Pi_{k+1} - \Pi_k$) as a function of the period for modes with $\ell = 1$ for He- (top panels) and hybrid-core (bottom panels) models, with stellar mass 0.338 $M_\odot$. Each column corresponds to a different H-envelope mass. In each plot, we show the period spacing for four effective temperatures along the cooling sequence, 12 000, 11 000, 10 000, and 9000 K.

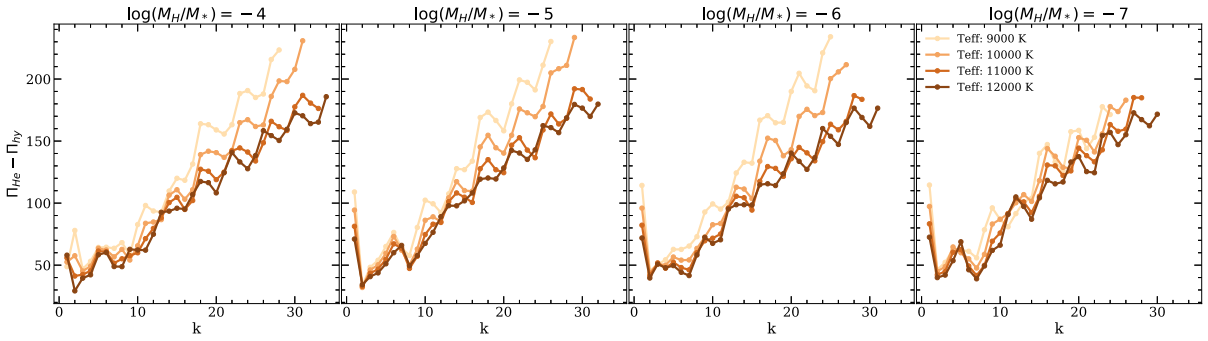

Figure 8. Period difference ($\Pi_{\rm he} - \Pi_{\rm hy}$) as a function of the radial order for $\ell = 1$ modes. The stellar mass is fixed to 0.338 $M_\odot$. Each plot corresponds to a different H-envelope mass. We consider four effective temperatures.

In general, we expect the forward period spacing to increase with decreasing effective temperature and thinner envelopes (Brassard et al. 1992b). This can be better explained in terms of the asymptotic period spacing, given by equation (6). The higher values for $\Delta\Pi_a$, and $\overline{\Delta\Pi}$, for lower effective temperatures result from the dependence of the Brunt-Väisälä frequency as $N \propto \sqrt{\chi_T}$, with $\chi_T \rightarrow 0$ for increasing degeneracy ($T \rightarrow 0$) (see for instance Romero et al. 2012). In addition, the asymptotic period spacing, and the mean period spacing, are longer for thinner H envelopes (Tassoul et al. 1990).

If the stellar mass is fixed, the asymptotic period spacing for the He-core model is longer than that for the hybrid-core model, for the same effective temperature and H-envelope mass. This is related to the dependence of the Brunt-Väisälä frequency on the surface gravity $N \propto g$, where $g \propto M/R^2$. In this case, the radius is smaller for the hybrid-core models which leads to a larger value of the surface gravity (see Figs 3 and 4).

Finally, given the different chemical structure of He- and hybrid-core WD models, we expect different values for the period spectra as well. Fig. 8 shows the period difference between He- and the hybrid-core models, $\Pi_{\rm he} - \Pi_{\rm hy}$ as a function of the radial order k, for harmonic degree $\ell = 1$. Each column corresponds to a different H-envelope mass, while the curves in each panel correspond to four different effective temperatures along the 0.338 $M_\odot$ WD cooling track. In all cases, the difference in the periods between the He- and hybrid-core models are between ∼50 s, for $k \lesssim 10$ and short periods, and ∼200 s for $k \gtrsim 30$ and longer periods. Note that the period difference is always positive, meaning that, for a given radial order, the period for the He-core model is larger than the one corresponding to the hybrid-core model. This is expected, since the periods, and the period spacing, vary as the inverse of the Brunt-Väisälä frequency, and thus the surface gravity (equation 7). As the period also increases with the cooling age, the period difference is larger for lower effective temperatures, particularly for modes with radial order $k > 20$. For future reference, we list the periods for $\ell = 1$ and $\ell = 2$, corresponding to the models considered in Fig. 8 and in Tables A1–A4.

4.2 Asteroseismology of J1152+0248 −V

For J1152+0248 −V Parsons et al. (2020) detected three pulsation periods, with the period of ∼1314 s being the one showing the highest amplitude. The list of observed periods and their corresponding amplitudes are listed in Table 2.

In order to find the theoretical model that better matches the observed periods, we use a standard χ^2 approach where we search for a minima of the quality function, defined as

$$\chi^2 = \sum_{i=1}^{3} \left(\frac{\Pi_{\rm obs}^{(i)} - \Pi_{\rm th}^{(i)}}{\sigma_{\rm obs}^{(i)}} \right)^2 , \qquad (8)$$

where $\Pi_{\rm obs}^{(i)}$ and $\sigma_{\rm obs}^{(i)}$ are the observed periods and their associated uncertainties in g_s-band, and $\Pi_{\rm th}^{(i)}$ are the theoretical periods. In our fit, we consider the mode with the highest detected amplitude, as an $\ell = 1$ mode, since the amplitude is expected to decrease with increasing harmonic degree due to geometric cancellation (Robinson, Kepler & Nather 1982). For the remaining two observed periods, we allowed them to be fitted by $\ell = 1$ and $\ell = 2$ modes. Finally, we restrict the possible seismological solutions to those models that fit the observed periods within the uncertainties reported by Parsons et al. (2020; see Table 2). The results of our seismological fit are depicted in Fig. 9. The value of χ^2 (colour scale) is shown as a function of the effective temperature and the mass of the H envelope. Top (bottom) panels correspond to models with stellar mass 0.338 $M_\odot$ (0.325 $M_\odot$). Models with He core are depicted on the left-hand panels, while the ones with hybrid core are shown in the right-hand panels. The dashed-line rectangle indicates the region where the models are compatible with the radius and effective temperature determinations from Parsons et al. (2020). As can be seen from this figure, there are several families of solutions. For a stellar mass 0.325 $M_\odot$, the best-fitting models are mainly characterized by thick H envelopes, $\sim 10^{-4}$ $M_\odot$ and low effective temperatures, > 9 000 K, for both core compositions. Thin H-envelope solutions, with H mass below $\sim 10^{-5}$ $M_\odot$, are found for models with stellar mass 0.338 $M_\odot$ and hybrid core, for all the effective temperature range.

If we combine our seismological results with the restrictions from the radius and the effective temperature presented in Parsons et al. (2020) (dashed-line rectangle in Fig. 9), the number of possible seismological solutions is largely reduced. In particular, the models characterized by a hybrid-core structure are the ones satisfying both criteria.

Table 2. Observed pulsation periods and the corresponding amplitudes for J1152+0248 −V (Parsons et al. 2020).

Period (s)	Amplitude (ppt)
1314 ± 5.9	33.0 ± 1.3
1069 ± 13	9.8 ± 1.3
582.9 ± 4.3	8.9 ± 1.3

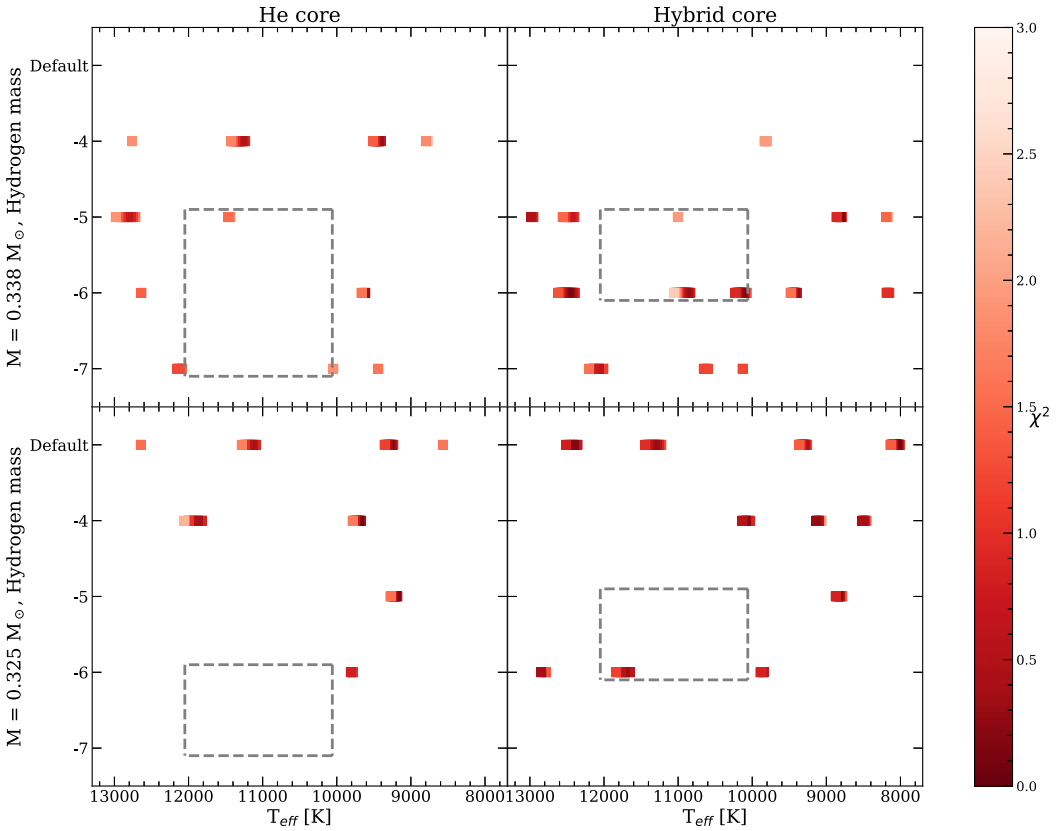

Figure 9. The value of χ^2 (colour scale) as a function of the effective temperature and the mass of the H envelope. Top panels correspond to models with stellar mass 0.338 $M_\odot$, while bottom panels show the results for 0.325 $M_\odot$ models. Both He- (left-hand panels) and hybrid-core (right-hand panels) structures are considered. The dashed-line rectangle indicates the region of the $T_{\rm eff}$–H envelope plane restricted by the determinations of radius and effective temperature from Parsons et al. (2020).

Table 3. Asteroseismological models for the low-mass WD J1152+0248 −V. The effective temperature, H-envelope mass, and central composition are listed in columns 2, 3, and 4, respectively. We list the theoretical periods that better fit the observed periods in column 4, along with the values of ℓ and k, in columns 6 and 7. The value of the quality function χ^2 is listed in column 8.

#	$T_{\rm eff}$ (K)	$R/R_\odot$	$M_*/M_\odot$	$M_H/M_\odot$	X_C	$\Pi_{\rm th}$ (s)	ℓ	k	χ^2 (s)
1	10 917	0.0187	0.338	10^{-6}	C/O	1315.4	1	21	0.296
						1063.3	2	30	–
						582.01	2	15	–
2	10 904	0.0187	0.338	10^{-6}	C/O	1316.1	1	21	0.305
						1063.8	2	30	–
						582.3	2	15	–
3	10 929	0.0187	0.338	10^{-6}	C/O	1314.9	1	21	0.318
						1062.8	2	30	–
						581.8	2	15	–
4	11 717	0.0195	0.325	10^{-6}	C/O	1316.1	1	21	0.345
						1066.4	2	30	–
						581.3	2	15	–

The best-fitting models for J1152+0248 −V are listed in Table 3. These models fit the observed periods within the uncertainties and are in agreement with the determinations of radius and effective temperature presented by Parsons et al. (2020). Note that all the models are characterized by an H-envelope mass of 10^{-6} $M_\odot$ and a hybrid core. Thus, we can conclude that J1152+0248 −V is a low-mass WD star with a hybrid core and a thin H envelope.

5 CONCLUSIONS

In this work, we explore the inner chemical structure of the pulsating low-mass WD in the J1152+0248 system using asteroseismology as a tool. This is the first pulsating low-mass WD in an eclipsing binary system with another low-mass WD which allows constraining the mass and radius of each component independently of evolutionary models.

We use low-mass WDs models with a stellar mass of 0.325 and 0.338 $M_\odot$ and an He core and hybrid core, respectively, resulting from fully binary evolutionary computations. In addition, to account for the uncertainty in the H-envelope mass due to the evolution through a common-envelope channel, we use WD sequences with the same stellar mass but with an H envelope thinner than the canonical value obtained from stable mass transfer, i.e. from 10^{-4} to 10^{-10} $M_\odot$. For all these sequences, we calculate adiabatic pulsations for effective temperatures in the range 13 000 K $\leq T_{\rm eff} \leq$ 8000 K.

We perform a study on the pulsating low-mass WD in the binary system J1152+0248 to uncover its inner chemical composition. By comparing the determinations of the radius and effective temperature presented by Parsons et al. (2020) with theoretical models (Istrate et al., in preparation), we find that the variable component of J1152+0248 must have an H envelope thinner than that predicted from stable mass-transfer binary evolution computations.

From the asteroseismological study we find a best-fitting model characterized by $M_* = 0.338$ $M_\odot$, $T_{\rm eff} = 10\,917$ K, $M_{\rm H}/M_\odot = 10^{-6}$, and a hybrid-core composition. In particular, all local minima of χ^2 correspond to models with hybrid core and a thin H envelope.

A systematic study of the pulsational properties and the observed period spectrum of low-mas WDs can give valuable information on the inner structure of these objects. This will help in disentangling the two WD populations coexisting in the mass interval ∼0.32–0.45 $M_\odot$ which in turn leads to clues of the underlying progenitor population.

ACKNOWLEDGEMENTS

ADR and GRL acknowledge the support of the Coordenação de Aperfeiçoamento de Pessoal de Nível Superior – Brazil (CAPES) – Finance Code 001, and by Conselho Nacional de Desenvolvimento Científico e Tecnológico - Brazil (CNPq). AGI acknowledges support from the Netherlands Organisation for Scientific Research (NWO). SGP acknowledges the support of a Science and Technology Facilities Council (STFC) Ernest Rutherford Fellowship. Special thanks to Pablo Marchant, Josiah Schwab, and Jocelyn Goldstein for their help with numerical debugging and to the developers of `MESA` and `GYRE` for their continuous efforts to improve and extend these codes. This research has made use of NASA's Astrophysics Data System and open source software such as the `Python 3` language (Python Core Team 2015), the IPYTHON KERNEL (Pérez & Granger 2007), the Jupyter Project (Kluyver et al. 2016), and the packages MATPLOTLIB (Hunter 2007), PANDAS (McKinney 2010), and the SCIPY ecosystem (Virtanen et al. 2019).

DATA AVAILABILITY

As an effort to promote open science, the results and codes to reproduce our results are available at https://zenodo.org/communities/mesa/.

REFERENCES

Althaus L. G., Córsico A. H., Isern J., García-Berro E., 2010a, A&AR, 18, 471
Althaus L. G., Córsico A. H., Bischoff-Kim A., Romero A. D., Renedo I., García-Berro E., Miller Bertolami M. M., 2010b, ApJ, 717, 897
Althaus L. G., Miller Bertolami M. M., Córsico A. H., 2013, A&A, 557, A19

Bell K. J., Kepler S. O., Montgomery M. H., Hermes J. J., Harrold S. T., Winget D. E., 2015, in Dufour P., Bergeron P., Fontaine G., eds, ASP Conf. Ser. Vol. 493, SDSS J1618+3854: The Sixth Extremely Low-Mass White Dwarf Pulsator. Astron. Soc. Pac., San Francisco, p. 217
Bell K. J. et al., 2017, ApJ, 835, 180
Bognar Z., Sodor A., 2016, Inf. Bull. Var. Stars, 6184, 1
Bradley P. A., Winget D. E., Wood M. A., 1993, ApJ, 406, 661
Brassard P., Fontaine G., Wesemael F., Kawaler S. D., Tassoul M., 1991, ApJ, 367, 601
Brassard P., Fontaine G., Wesemael F., Hansen C. J., 1992a, ApJS, 80, 369
Brassard P., Fontaine G., Wesemael F., Tassoul M., 1992b, ApJS, 81, 747
Brickhill A. J., 1991, MNRAS, 251, 673
Cassisi S., Potekhin A. Y., Pietrinferni A., Catelan M., Salaris M., 2007, ApJ, 661, 1094
Chaboyer B., Zahn J. P., 1992, A&A, 253, 173
Córsico A. H., Althaus L. G., 2014, A&A, 569, A106
Córsico A. H., Althaus L. G., Benvenuto O. G., Serenelli A. M., 2002, A&A, 387, 531
Córsico A. H., Althaus L. G., Miller Bertolami M. M., Kepler S. O., 2019, A&AR, 27, 7
Cowling T. G., 1941, MNRAS, 101, 367
Dolez N., Vauclair G., 1981, A&A, 102, 375
Ferguson J. W., Alexander D. R., Allard F., Barman T., Bodnarik J. G., Hauschildt P. H., Heffner-Wong A., Tamanai A., 2005, ApJ, 623, 585
Fontaine G., Brassard P., 2008, PASP, 120, 1043
Fuchs J. T., 2017, PhD thesis, Univ. North Carolina at Chapel Hill
Garcia-Berro E., Isern J., Hernanz M., 1997, MNRAS, 289, 973
Goldreich P., Wu Y., 1999, ApJ, 511, 904
Grevesse N., Sauval A. J., 1998, Space Sci. Rev., 85, 161
Hallakoun N. et al., 2016, MNRAS, 458, 845
Han Z., Tout C. A., Eggleton P. P., 2000, MNRAS, 319, 215
Heger A., Langer N., Woosley S. E., 2000, ApJ, 528, 368
Henyey L., Vardya M. S., Bodenheimer P., 1965, ApJ, 142, 841
Hermes J. J. et al., 2013a, MNRAS, 436, 3573
Hermes J. J. et al., 2013b, ApJ, 765, 102
Hunter J. D., 2007, Comput. Sci. Eng., 9, 90
Iben I. J., Tutukov A. V., 1985, ApJS, 58, 661
Iglesias C. A., Rogers F. J., 1993, ApJ, 412, 752
Iglesias C. A., Rogers F. J., 1996, ApJ, 464, 943
Istrate A. G., Tauris T. M., Langer N., 2014, A&A, 571, A45
Istrate A. G., Marchant P., Tauris T. M., Langer N., Stancliffe R. J., Grassitelli L., 2016, A&A, 595, A35
Itoh N., Kohyama Y., Takeuchi H., 1987, ApJ, 317, 733
Kawaler S. D., 1988, ApJ, 333, 236
Kepler S. O., Kleinman S. J., Nitta A., Koester D., Castanheira B. G., Giovannini O., Costa A. F. M., Althaus L., 2007, MNRAS, 375, 1315

Kepler S. O. et al., 2015, MNRAS, 446, 4078
Kilic M., Stanek K. Z., Pinsonneault M. H., 2007, ApJ, 671, 761
Kilic M., Hermes J. J., Gianninas A., Brown W. R., 2015, MNRAS, 446, L26

Kluyver T. et al., 2016, in Loizides F., Schmidt B., eds, Positioning and Power in Academic Publishing: Players, Agents and Agendas. p. 87
Kupfer T. et al., 2019, ApJ, 878, L35
Langer N., Fricke K. J., Sugimoto D., 1983, A&A, 126, 207
Lauffer G. R., Romero A. D., Kepler S. O., 2018, MNRAS, 480, 1547
McKinney W., 2010, in van der Walt S., Millman J., eds, Proc. 9th Python Sci. Conf., Vol. 445, Data Structures for Statistical Computing in Python. p. 56
Panei J. A., Althaus L. G., Chen X., Han Z., 2007, MNRAS, 382, 779
Parsons S. G. et al., 2020, Nature Astron., 4, 690
Paxton B., Bildsten L., Dotter A., Herwig F., Lesaffre P., Timmes F., 2011, ApJS, 192, 3
Paxton B. et al., 2013, ApJS, 208, 4
Paxton B. et al., 2015, ApJS, 220, 15
Paxton B. et al., 2018, ApJS, 234, 34
Paxton B. et al., 2019, ApJS, 243, 10
Pelisoli I., Vos J., 2019, MNRAS, 488, 2892
Pelisoli I., Kepler S. O., Koester D., Castanheira B. G., Romero A. D., Fraga L., 2018, MNRAS, 478, 867
Pérez F., Granger B. E., 2007, Comput. Sci. Eng., 9, 21

Pietrukowicz P. et al., 2017, Nature Astron., 1, 0166
Prada Moroni P. G., Straniero O., 2009, A&A, 507, 1575
Python Core Team, 2015, Python: A Dynamic, Open Source Programming Language. Python Software Foundation, Available at: https://www.python.org/
Robinson E. L., Kepler S. O., Nather R. E., 1982, ApJ, 259, 219
Rohrmann R. D., Althaus L. G., García-Berro E., Córsico A. H., Miller Bertolami M. M., 2012, A&A, 546, A119
Romero A. D., Córsico A. H., Althaus L. G., Kepler S. O., Castanheira B. G., Miller Bertolami M. M., 2012, MNRAS, 420, 1462
Romero A. D., Campos F., Kepler S. O., 2015, MNRAS, 450, 3708
Romero A. D. et al., 2019, MNRAS, 490, 1803
Rowan D. M., Tucker M. A., Shappee B. J., Hermes J. J., 2019, MNRAS, 486, 4574
Su J., Fu J., Lin G., Chen F., Khokhuntod P., Li C., 2017, ApJ, 847, 34
Tassoul M., Fontaine G., Winget D. E., 1990, ApJS, 72, 335
Thoul A. A., Bahcall J. N., Loeb A., 1994, ApJ, 421, 828
Townsend R. H. D., Teitler S. A., 2013, MNRAS, 435, 3406
Townsend R. H. D., Goldstein J., Zweibel E. G., 2018, MNRAS, 475, 879
Unno W., Osaki Y., Ando H., Saio H., Shibahashi H., 1989, Nonradial Oscillations of Stars, 2nd edn. University of Tokyo Press, Tokyo
Virtanen P. et al., 2019, Nature Methods, 17, 261
Winget D. E., van Horn H. M., Tassoul M., Fontaine G., Hansen C. J., Carroll B. W., 1982, ApJ, 252, L65
Woosley S. E., Heger A., 2015, ApJ, 810, 34
Zenati Y., Toonen S., Perets H. B., 2019, MNRAS, 482, 1135

APPENDIX A: THEORETICAL PERIODS

Table A1. Period values for $\ell = 1$ and $\ell = 2$ modes corresponding to models with $M_* = 0.338$ $M_\odot$, effective temperature of 12 000 K, and H-envelope mass of 10^{-4}, 10^{-5}, and 10^{-6} $M_\odot$.

$M_H/M_\odot$		10^{-4}		10^{-5}		10^{-6}	
ℓ	k	He	C/O	He	C/O	He	C/O
1	1	204.948	146.886	218.643	147.610	220.319	148.418
1	2	221.260	192.002	273.896	239.660	291.871	252.223
1	3	292.114	252.597	296.524	255.774	356.006	305.175
1	4	364.331	322.131	369.816	326.066	376.420	328.547
1	5	420.666	362.298	442.175	391.085	442.595	392.939
1	6	465.821	405.630	507.842	447.835	512.597	468.370
1	7	518.050	469.162	560.626	494.718	583.536	541.930
1	8	578.586	529.785	606.713	557.217	650.957	592.739
1	9	636.102	573.359	665.303	607.547	704.944	632.512
1	10	682.723	620.481	727.082	659.543	752.211	684.640
1	11	739.842	677.741	786.677	710.230	810.293	739.861
1	12	798.462	723.525	838.796	749.740	873.722	778.522
1	13	849.341	756.759	892.586	794.649	937.811	838.306
1	14	902.294	808.744	954.758	856.940	997.247	898.565
1	15	960.397	864.535	1014.63	912.796	1051.18	952.676
1	16	1014.40	919.221	1067.36	959.175	1106.24	991.396
1	17	1066.15	959.235	1122.26	1002.96	1168.11	1052.52
1	18	1122.16	1004.73	1182.63	1062.39	1231.03	1116.87
1	19	1177.61	1061.12	1240.57	1121.12	1289.88	1166.22
1	20	1229.32	1121.06	1294.31	1165.97	1343.50	1203.20
2	1	120.014	100.316	141.344	100.940	142.736	101.493
2	2	142.587	111.277	160.508	139.347	185.489	150.999
2	3	185.975	151.547	187.659	152.494	209.625	176.847
2	4	225.657	191.494	231.584	194.754	232.453	195.717
2	5	254.034	211.840	272.358	229.803	273.019	231.131
2	6	281.506	237.353	307.956	260.380	314.097	273.528
2	7	314.200	273.648	334.955	288.159	354.935	316.423
2	8	349.925	308.696	364.899	326.241	319.257	347.570
2	9	379.496	336.314	400.421	358.342	418.988	372.001
2	10	408.479	365.660	435.919	386.702	449.058	401.706
2	11	443.206	396.338	468.693	416.106	484.623	439.694
2	12	475.033	425.943	497.913	452.092	521.580	476.215
2	13	504.023	461.149	531.857	483.738	557.625	498.294
2	14	536.607	486.195	567.956	503.483	590.826	524.268
2	15	569.643	506.188	600.466	533.089	621.325	560.439
2	16	599.506	538.593	630.662	570.281	655.268	596.169
2	17	630.599	572.313	664.302	597.936	691.754	617.974
2	18	663.345	594.209	699.097	619.426	727.368	649.520
2	19	694.175	617.784	731.092	652.467	759.583	684.916
2	20	724.441	652.464	762.392	689.291	791.026	716.668
2	21	756.787	684.847	795.637	714.925	825.950	738.317
2	22	787.930	709.047	829.417	737.077	861.764	774.935
2	23	818.226	731.327	861.601	772.178	895.634	813.010
2	24	849.940	764.288	893.184	810.806	927.753	848.125
2	25	881.227	800.000	926.496	843.600	960.895	870.022
2	26	911.804	833.115	959.922	863.817	995.764	902.046
2	27	943.122	853.700	991.721	894.125	1030.54	939.114
2	28	974.435	879.080	1023.75	930.100	1063.74	966.625
2	29	1005.23	913.682	1057.21	956.318	1096.41	989.506
2	30	1036.10	941.506	1089.98	978.538	1130.42	1026.26

Table A2. Period values for $\ell = 1$ and $\ell = 2$ modes corresponding to models with $M_* = 0.338$ M$_\odot$, effective temperature of 11 000 K, and H-envelope mass of 10^{-4}, 10^{-5}, and 10^{-6} M$_\odot$.

$M_H/M_\odot$		10^{-4}		10^{-5}		10^{-6}	
ℓ	k	He	C/O	He	C/O	He	C/O
1	1	207.777	151.919	233.957	152.645	235.524	153.322
1	2	234.935	193.714	276.833	243.947	307.762	266.071
1	3	308.929	266.516	311.893	268.497	361.733	309.919
1	4	380.793	335.386	389.048	342.310	391.382	343.863
1	5	433.845	372.487	463.274	408.527	463.749	411.409
1	6	481.618	420.763	528.221	461.074	537.098	489.063
1	7	538.336	486.755	577.219	513.621	610.573	564.377
1	8	602.632	547.503	629.465	582.118	676.213	616.106
1	9	655.766	598.093	692.730	635.549	725.608	655.982
1	10	707.296	647.314	756.426	681.750	779.270	707.562
1	11	769.074	697.705	814.497	731.479	843.416	768.330
1	12	825.765	746.133	866.850	782.429	909.524	813.564
1	13	877.491	789.346	928.721	827.532	973.853	868.318
1	14	936.544	836.128	992.887	884.697	1032.09	927.724
1	15	994.745	890.138	1049.75	944.978	1087.01	992.624
1	16	1047.83	952.948	1104.48	1003.92	1149.66	1032.11
1	17	1104.56	1002.48	1166.22	1038.52	1215.34	1085.88
1	18	1162.76	1035.48	1227.62	1092.55	1277.54	1149.55
1	19	1216.77	1091.03	1283.50	1156.59	1333.40	1211.86
1	20	1272.22	1153.26	1340.63	1216.10	1392.04	1256.28
2	1	120.711	103.726	149.787	104.375	151.814	104.829
2	2	151.834	112.262	162.269	141.279	194.448	158.655
2	3	195.703	159.298	197.606	160.112	211.759	179.466
2	4	234.191	198.316	243.168	203.875	243.337	204.548
2	5	261.843	218.039	284.536	239.630	285.963	241.754
2	6	291.547	246.112	318.537	267.939	328.974	285.360
2	7	327.190	283.652	345.423	299.045	370.474	328.794
2	8	362.990	318.254	379.569	339.961	404.184	360.358
2	9	390.988	350.257	416.755	375.420	431.958	388.493
2	10	424.473	383.250	452.823	402.049	466.541	417.648
2	11	459.804	409.554	483.925	429.733	504.598	454.562
2	12	490.304	438.938	516.320	467.240	542.571	490.865
2	13	521.968	475.075	553.706	498.686	578.574	513.862
2	14	556.885	500.928	589.250	519.210	610.434	540.633
2	15	588.750	521.371	620.508	550.428	644.063	580.230
2	16	620.001	555.159	654.070	590.481	681.677	621.644
2	17	653.702	590.195	690.425	625.170	719.126	649.981
2	18	686.347	622.643	724.303	648.467	753.175	671.000
2	19	717.267	644.476	756.359	674.238	785.390	707.347
2	20	750.538	671.115	790.585	711.447	821.198	745.512
2	21	783.051	704.597	825.706	743.906	858.469	768.119
2	22	814.218	737.499	859.058	764.570	893.692	799.575
2	23	846.959	757.240	891.796	797.047	926.893	838.324
2	24	879.365	785.944	926.331	835.814	961.390	878.146
2	25	911.008	822.649	960.885	872.099	997.639	907.292
2	26	943.351	858.165	993.755	900.244	1033.59	933.155
2	27	975.716	887.886	1027.15	924.922	1067.91	970.154
2	28	1007.49	908.910	1061.95	960.303	1101.84	1008.85
2	29	1072.09	940.675	1095.65	997.176	1137.52	1034.44
2	30	1103.79	975.775	1128.77	1024.26	1173.68	1060.13

Table A3. Period values for $\ell = 1$ and $\ell = 2$ modes corresponding to models with $M_* = 0.338$ M$_\odot$, effective temperature of 10 000 K, and H-envelope mass of 10^{-4}, 10^{-5}, and 10^{-6} M$_\odot$.

$M_H/M_\odot$		10^{-4}		10^{-5}		10^{-6}	
ℓ	k	He	C/O	He	C/O	He	C/O
1	1	209.850	157.321	252.328	157.951	254.801	158.549
1	2	253.518	195.924	280.175	248.189	326.917	283.059
1	3	329.045	283.798	331.577	285.471	366.984	315.927
1	4	398.872	349.747	411.843	361.596	412.719	362.727
1	5	449.743	386.155	487.861	248.295	490.081	433.524
1	6	501.311	439.089	550.052	476.945	567.284	513.238
1	7	564.292	507.595	598.176	536.112	642.441	588.261
1	8	629.238	566.539	658.379	608.287	703.193	639.718
1	9	679.188	625.059	725.480	662.554	752.760	680.114
1	10	739.471	673.875	790.184	704.021	815.755	733.170
1	11	802.594	718.873	845.394	756.443	884.549	800.999
1	12	856.823	772.083	904.980	819.879	953.196	856.930
1	13	914.781	828.101	972.970	868.674	1017.90	905.083
1	14	977.584	871.154	1036.10	918.761	1075.56	964.206
1	15	1034.07	923.283	1092.89	982.771	1138.42	1034.76
1	16	1091.60	988.449	1155.57	1045.98	1208.10	1074.30
1	17	1153.16	1042.38	1222.19	1076.96	1277.21	1124.88
1	18	1211.49	1072.43	1284.28	1129.61	1341.23	1190.77
1	19	1268.95	1127.11	1344.28	1199.66	1402.32	1264.19
1	20	1330.48	1189.77	1408.16	1267.85	1468.56	1325.45
2	1	121.586	107.287	157.518	107.919	163.156	108.312
2	2	163.416	113.564	167.306	143.524	203.910	168.026
2	3	206.981	168.965	209.618	169.896	216.181	183.062
2	4	243.544	205.790	256.828	214.873	257.004	215.468
2	5	271.659	226.439	298.421	250.869	302.091	254.650
2	6	304.270	256.870	329.841	277.285	347.023	299.360
2	7	343.101	295.672	359.639	312.151	388.134	342.354
2	8	376.609	329.099	397.374	355.056	418.378	374.155
2	9	406.703	365.975	436.177	392.490	450.250	406.368
2	10	443.943	400.944	471.367	418.069	489.031	434.251
2	11	478.181	424.514	502.886	445.030	529.062	470.434
2	12	509.339	453.685	540.512	483.040	568.103	506.993
2	13	545.056	489.279	579.302	514.825	603.410	532.999
2	14	580.024	516.482	613.501	538.859	637.183	562.265
2	15	612.022	540.797	647.314	572.300	675.967	604.029
2	16	646.904	574.901	685.322	612.391	716.491	646.414
2	17	981.976	609.741	722.939	649.241	755.304	682.219
2	18	714.771	647.571	757.683	684.100	790.917	702.311
2	19	749.324	679.309	793.296	703.049	827.350	735.388
2	20	784.642	696.728	831.114	737.108	866.985	777.381
2	21	818.136	728.585	868.816	774.163	907.360	807.014
2	22	852.723	764.778	904.819	802.704	946.459	832.156
2	23	888.137	792.796	941.137	828.950	984.102	871.453
2	24	922.537	815.698	979.211	866.280	1021.99	914.490
2	25	957.299	850.262	1017.29	905.561	1061.17	951.177
2	26	992.689	887.230	1053.93	942.024	1101.43	976.345
2	27	1027.87	923.354	1090.87	966.846	1141.57	1011.69
2	28	1062.61	950.145	1129.15	998.759	1180.46	1053.86
2	29	1098.14	975.476	1167.12	1038.43	1219.08	1088.51
2	30	1133.72	1011.07	1204.56	1074.88	1258.10	1110.10

Table A4. Period values for $\ell = 1$ and $\ell = 2$ modes corresponding to models with $M_* = 0.338\ M_\odot$, effective temperature of **9 000** K, and H-envelope mass of 10^{-4}, 10^{-5}, and $10^{-6}\ M_\odot$.

$M_H/M_\odot$		10^{-4}		10^{-5}		10^{-6}	
ℓ	k	He	C/O	He	C/O	He	C/O
1	1	211.971	163.184	272.688	163.728	278.506	164.253
1	2	276.632	198.670	286.577	253.161	349.212	303.724
1	3	352.387	305.461	355.981	307.717	375.098	324.564
1	4	418.508	365.398	439.196	385.267	440.661	386.324
1	5	469.126	404.819	516.118	451.060	523.307	460.588
1	6	526.313	461.883	573.907	497.554	604.686	542.008
1	7	595.997	532.423	627.193	563.328	680.545	615.165
1	8	657.552	589.357	695.003	637.210	738.264	665.314
1	9	711.747	653.526	766.831	686.424	797.295	704.490
1	10	780.216	697.500	833.735	731.373	868.130	768.783
1	11	843.534	745.433	893.015	793.537	942.846	847.662
1	12	901.897	808.247	961.966	869.583	1019.19	918.324
1	13	968.255	875.514	1036.37	928.897	1094.93	970.636
1	14	1035.46	925.732	1106.85	979.084	1164.70	1031.76
1	15	1097.32	977.308	1172.29	1045.33	1233.01	1100.78
1	16	1162.30	1043.90	1241.03	1107.19	1306.57	1139.70
1	17	1230.74	1099.27	1314.57	1145.56	1383.92	1213.45
1	18	1296.20	1132.24	1387.83	1214.51	1462.30	1297.58
1	19	1360.81	1197.61	1458.53	1291.93	1539.71	1374.64
1	20	1429.04	1270.06	1527.91	1369.63	1614.85	1424.85
2	1	122.673	111.022	161.731	111.709	177.473	112.048
2	2	177.534	115.239	179.106	146.305	211.221	178.889
2	3	219.601	181.074	224.211	182.664	226.761	188.896
2	4	254.109	214.244	273.063	228.523	274.394	229.265
2	5	283.806	237.817	313.728	263.906	322.327	270.651
2	6	320.563	270.466	343.764	289.721	369.126	316.276
2	7	361.292	310.114	378.605	328.255	408.989	358.240
2	8	392.415	342.644	419.762	372.913	440.332	391.682
2	9	428.280	384.076	460.811	410.346	478.305	423.698
2	10	467.738	417.823	496.879	433.479	507.736	451.141
2	11	502.082	439.454	532.901	463.571	564.517	493.970
2	12	537.746	471.766	575.233	507.100	608.865	537.519
2	13	577.290	510.640	617.606	544.610	651.321	570.193
2	14	614.507	543.309	656.751	574.361	690.583	602.753
2	15	650.556	573.042	694.888	610.217	731.419	647.504
2	16	689.501	608.268	736.295	655.098	775.176	697.196
2	17	728.692	646.436	779.002	698.230	820.347	733.340
2	18	765.618	688.715	820.721	730.570	865.547	756.089
2	19	804.125	724.033	861.022	752.829	909.721	799.923
2	20	843.683	741.825	901.474	797.069	952.601	844.521
2	21	882.106	778.876	943.447	839.523	995.140	871.128
2	22	920.408	820.648	986.213	865.190	1038.45	909.888
2	23	959.520	851.564	1028.20	898.880	1082.74	959.228
2	24	998.867	876.304	1069.13	645.024	1127.70	1003.20
2	25	1037.62	916.100	1110.60	988.842	1172.86	1032.01
2	26	1076.42	958.321	1153.10	1019.67	1217.46	1070.84
2	27	1116.01	995.860	1195.53	1052.01	1261.71	1117.93
2	28	1155.22	1022.68	1237.56	1095.90	1305.52	1157.13
2	29	1194.12	1057.21	1279.30	1137.63	1349.21	1187.67
2	30	1233.58	1097.80	1321.30	1166.17	1393.53	1231.34

This paper has been typeset from a TEX/LATEX file prepared by the author.